

Synergizing Structural Stiffness Regulation with Compliance Contact Stiffness: Bioinspired Soft Stimuli-Responsive Materials Design for Soft Machines

Ke Ma, Jie Zhang, Ruotong Sun, Binhan Chang, Siyuan Zhang, Xiaojun Wang,* Jianing Wu,* and Jinxiu Zhang*

Stiffness regulation strategies endow soft machines with stronger functionality to cope with diverse application requirements, for example manipulating heavy items by improving structural stiffness. However, most programmable stiffness strategies usually struggle to preserve the inherent compliant interaction capabilities following an enhancement in structural stiffness. In this study, inspired by the musculocutaneous system, we propose a soft stimuli-responsive material (SRM) by combining shape memory alloy into compliant materials. By characterizing the mechanical performance, the flexural modulus increases from 6.6 to 142.4 MPa under the action of active stimuli, crossing two orders of magnitude, while Young's modulus stays at 2.2 MPa during programming structural stiffness. This comparative result indicates that our SRMs can keep a lower contact stiffness for compliant interaction although structural stiffness increases. Then, we develop three diverse soft machines to show the application potential of this smart material, such as robotic grippers, wearable devices, and deployable mechanisms. By applying our materials, these machines possess stronger load-bearing capabilities. Meanwhile, these demonstrations also illustrate the efficacy of this paradigm in regulating the structural stiffness of soft machines while maintaining their compliant interaction capabilities.

more adaptable alternatives for applications that traditional rigid paradigms cannot handle.^[7,8] However, due to the limitation of structural stiffness, traditional soft machines are unable to cope with some application scenarios, particularly for manipulating heavy objects.^[9–12] To overcome this limitation, there is a need to devise an approach to enable the structural stiffness to be programmable for meeting diverse interaction requirements.^[13–16]

Recently, researchers have presented several stimuli-response materials that can achieve mechanical responses under the action of external fields,^[17–20] such as light,^[21] magnetic,^[22,23] and electric fields.^[24] Utilizing this distinctive feature of advanced materials, such as dielectric elastomers (DEs),^[25–27] low-melting-point alloys (LMPAs),^[28–30] and shape memory polymers (SMPs)^[31–35] to construct soft machines, can endow them with tunable structural stiffness. For instance, Aksoy et al. employed DEs to develop multimorph soft actuator sheets with enhanced load-

bearing capabilities, which could obtain multiple distinct configurations controlled by Joule heating.^[36] However, this material is susceptible to electrical breakdown due to its requirement for high driving voltage (in kV) and its vulnerability to leakage currents.^[37] To circumvent the challenges of high voltage, Zhang et al. combined elastic materials and LMPAs to present an intelligent spring with tunable stiffness and then introduced it into a continuum robot to provide a foundation for the application for interacting with unstructured environments.^[38] Nonetheless, the mechanical properties of LMPAs may be altered due to the reaction with the encapsulant, which may lead to unexpected issues, such as encapsulation deterioration and potential material permeation.^[39] Then, Mattmann et al. presented variable-stiffness robotic catheters which could enhance maneuverability and safety in various medical procedures. This design utilizes SMPs that are notable for their low actuation voltage and absence of leakage.^[35] However, prolonged exposure of SMPs to external tensile stress triggers a relaxation process, resulting in the irreversible plastic deformation of the sample due to the slippage and disentanglement of the polymer chains.^[40–42]

1. Introduction

Soft machines^[1] composed of compliant materials, such as robotic grippers, can conform to intricate geometries,^[2,3] mitigate shocks, and interact with biological systems,^[4–6] providing

K. Ma, J. Zhang, R. Sun, B. Chang, S. Zhang, J. Wu, J. Zhang
School of Aeronautics and Astronautics
Sun Yat-Sen University
Shenzhen 518107, P. R. China
E-mail: wujn27@mail.sysu.edu.cn; zhangjinxiu@sysu.edu.cn

X. Wang
Beijing Institute of Mechanical Equipment
Beijing 100076, P. R. China
E-mail: momolne@163.com

J. Wu
School of Advanced Manufacturing
Sun Yat-Sen University
Shenzhen 518107, P. R. China

 The ORCID identification number(s) for the author(s) of this article can be found under <https://doi.org/10.1002/adem.202400461>.

DOI: 10.1002/adem.202400461

In contrast to the aforementioned strategies based on advanced materials, the jamming method offers an alternative approach for regulating the structural stiffness of soft machines^[43–46]. For example, Shah et al. created thin and reconfigurable “jamming skins” to regulate the stiffness of soft machines, encompassing the calibration of soft robotic arm trajectories, functioning as dynamic wrist support, and constructing intricate architectures as required.^[47] Li et al. proposed a design using a pack (made of strain-limiting membrane) of particles to stiffen a soft actuator. Using passive particle jamming, the actuator exhibits more than six folds in stiffness variation using the prototype.^[48] Moreover, the membrane presses the elements together and interlayer friction prevents further sliding, thus increasing higher contact stiffness, making the skin stiff and inextensible. However, this stiff state hinders the adaptability of soft machine applications, particularly in interacting with living organisms or manipulating delicate items.^[49,50] As shown in Figure 1A, the conventional method of regulating stiffness compromises contact stiffness while enhancing structural stiffness. There is a pressing demand for a design that not only enhances structural stiffness but maintains compliant interaction capabilities for soft machines.

Biological organisms leverage a wide range of material properties to adapt to various environments.^[51,52] In this study, drawing inspiration from the musculocutaneous system,^[53] we propose a stimuli-responsive material (SRM), which exhibits a compliant interaction interface and a capability of actively regulating structural stiffness. Here, these SRMs are embedded with stiffness-programmable composites coupled with compliant materials, effectively reconciling the challenges posed by trade-offs between compliant interaction and load-bearing capability. To comply with variable-application scenarios, we arrange four shape memory alloys (SMA) patterns in the silicon substrate, as shown in Figure 1B, namely Patterns 1, 2, 3, and 4. By applying Joule heat to these SRMs, these materials can rapidly transition to a rigid state within 2.0 min, during which the flexural modulus switches from 6.6 to 142.4 MPa. To showcase the

application potential of our materials, we employ these soft materials to construct three soft machines, including a robotic gripper for grasping diverse objects, a wearable device for immobilizing injured limbs, and a deployable mechanism for disaster relief. This simple yet efficient material with tunable stiffness serves as the cornerstone for constructing soft machines, offering an approach that enhances load-bearing capacities and enriches interactive functionalities in next-generation soft machines.

2. Experimental Section

2.1. Fabrication of SRMs

The fabrication details are illustrated in Figure 2B; we amalgamated the constituent parts A and B of silicon rubber (Dragon Skin 30, Smooth-On, USA) in a stoichiometric 1:1 ratio by weight. To obviate potential structural effects induced by air bubbles, we subjected the composite to a vacuum pump for efficient degassing. Thereafter, we configured the SMA (8995, Gee SMA Technology Co. LTD, China) pattern within a mold, precision printed by 3D Printers (Shape 1+, Rayshape, China), and infused the silicone composite via a syringe. After a curing duration of 6-h interval, the silicon substrate and SMA achieved seamless integration. We subsequently removed it from the mold and straightened its structure via electrical stimuli. Next, we rotated it by 180 degrees, ensuring that the exposed facet of the SMA was oriented upward, positioned within a deeper mold, and additional silicone was introduced using a syringe again. Finally, after an additional 6-h interval, we gained the final SRM and performed electrical stimulation to achieve its desired straightening.

2.2. Surface Temperature Measurement

The surface temperature of SRMs was recorded using an infrared imaging device (K20, HIKVISION, China). Subsequently, the acquired thermal imagery underwent analytical processing

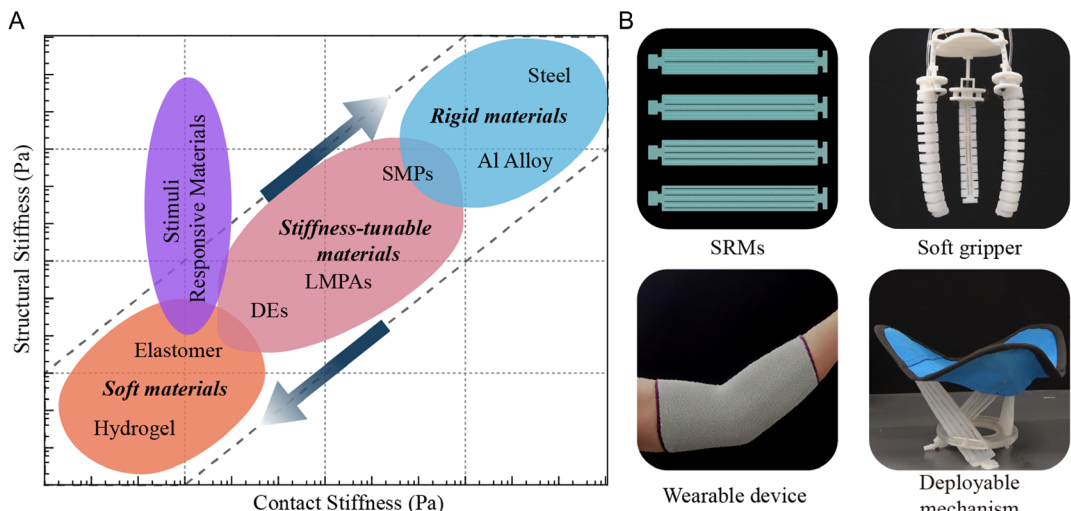


Figure 1. Stiffness properties and application demonstrations of SRMs. A) Relationship between maximum structural stiffness and contact stiffness of diverse materials, including soft, stiffness-tunable, rigid materials, and our SRMs. B) SRMs and three application demonstrations.

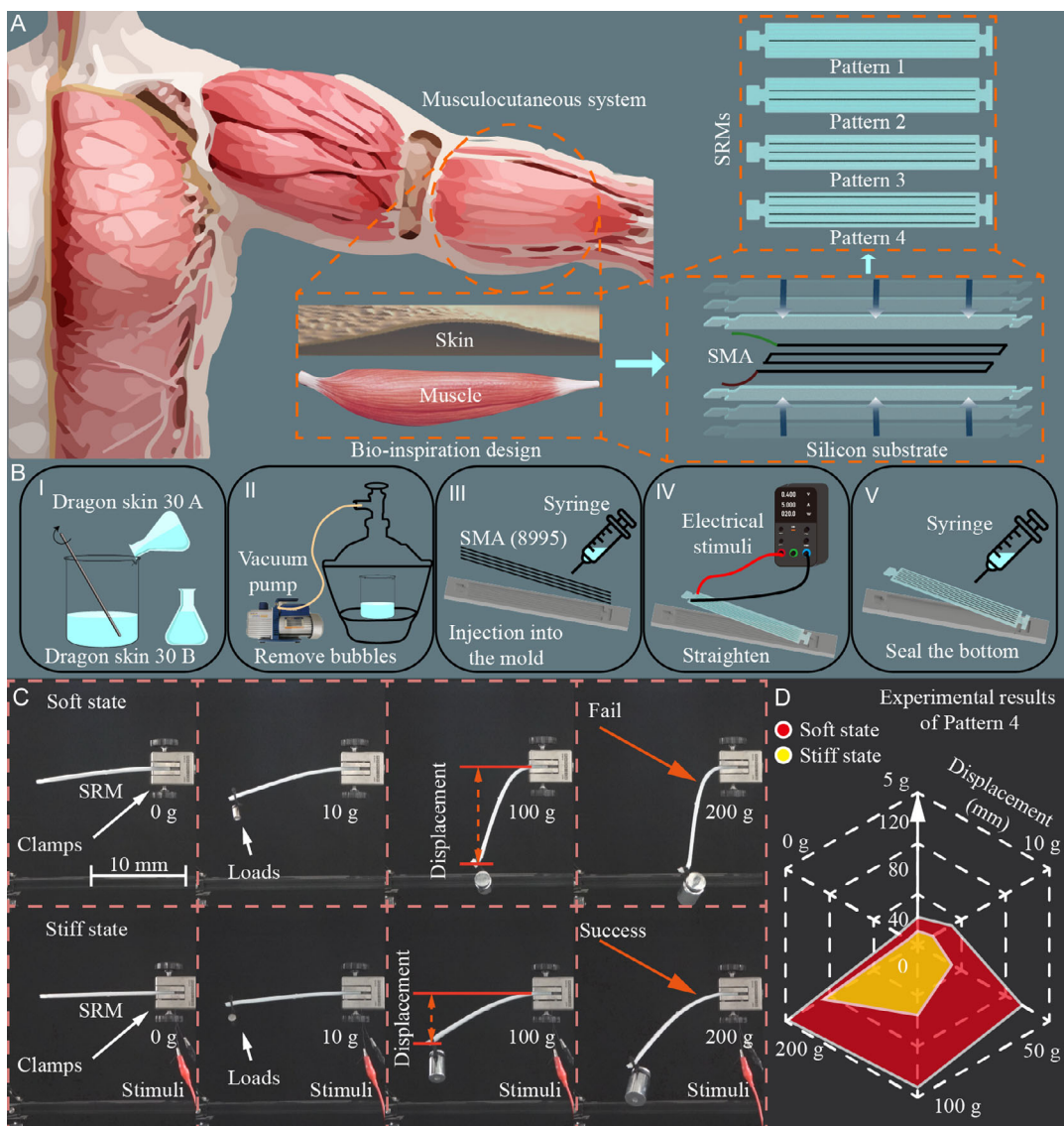


Figure 2. Biomimetic design, fabrication, and deformation performance of SRMs. A) Bioinspired SRM design. Inspired by the musculocutaneous system, the SRM is designed as a three-layer structure. Four patterns are designed namely Patterns 1–4. B) Fabrication process of the SRM. We utilized 3D-printed and soft lithography methodologies to fabricate SRM, and the detailed information is shown in I–V, respectively. C) Load-bearing deformation performance. Varying weights are loaded on the tip of SRM, and the longitudinal displacement is measured. D) Comparison between the soft and stiff states of Pattern 4.

through the specialized software, HIKMICRO Analyzer (HIKVISION, China).

2.3. Differential Scanning Calorimetry Analysis

In our endeavor to quantitatively evaluate the phase transition in SRM, differential scanning calorimetry (DSC) was employed to ascertain the SMA phase transition temperature. The sample for DSC analysis was meticulously sectioned to lengths of ≈ 10 mm utilizing a diamond saw, followed by encapsulation in a DSC pan. Dimensional fluctuations within the composites were evaluated using a thermomechanical analyzer (DZ-DSC30C,

Nanjing Dazhan Testing Instrument, China), operating at a controlled thermal ramp of $10\text{ }^{\circ}\text{C min}^{-1}$. The analysis was conducted under a nitrogen atmosphere, with the temperature protocol spanning from 0 to $100\text{ }^{\circ}\text{C}$ and subsequently reducing to $5\text{ }^{\circ}\text{C}$.

2.4. Three-Point Bending

For the three-point bending measurement of SRM specimens, each sample was aligned between an indenter and a pair of supports, maintaining a distance of 50 mm, as illustrated in Figure 4A. In preparation for testing, the SRMs were conditioned to attain thermal equilibrium with ambient room temperature

(25 °C). We applied an indenter to provide a vertical compressive force, which enabled the sample to deform. Dimensional specifics of the SRM samples included: a total length of 190 mm, an effective length of 150 mm, a thickness of 4 mm, and a breadth of 27.5 mm. Force responses were quantified using a MARK-10 tensile testing machine, with the dynamometer advancing at a controlled rate of 2 mm min⁻¹, culminating in a maximum displacement of 20 mm and exerting a peak force of 48 N. The experimental data were calculated, analyzed, and fitted by the software origin.

2.5. Contact Stiffness

To evaluate the contact stiffness of SRM samples, the preparation process commenced by equilibrating the SRM to ambient room temperature; subsequently, Joule thermal excitation was applied as required during the measurement phase. Here, we prepared three samples, including two SRMs respectively in soft and rigid states and a silicone substrate without any SMAs. Then, each sample was positioned horizontally on the support platform, ensuring alignment of its center with the pressure sensor. Uniaxial compression experiments on SRMs were conducted utilizing an ESM303 apparatus, fit with a 50 N load cell (ESM303, Mark-10, USA), to quantify the lateral contact stiffness. The sensor progressed at a controlled rate of 2 mm min⁻¹, culminating

in a peak stress of 48 N. Experimental data were also processed by the software origin.

3. Results and Discussion

3.1. Design of Bioinspired Materials with Tunable Stiffness

Biological systems consistently illuminate the intricate interplay between structure and function, presenting groundbreaking ideas that enhance the evolution of science and technology in the field of artificial soft robotics.^[54] For example, muscular structures harness chemical energy to facilitate diverse contractile responses and manifest differential rigidity between their passive (minimized stiffness) and active (maximized stiffness) states, enabling the modulation of both power and rigidity.^[55] Meanwhile, the dermis, constituted of collagen and elastic fibers situated exterior to the muscle, furnishes adaptable interaction proficiencies (Figure 2A).^[56] This biological paradigm may provide inspiration for the development of intelligent materials tailored to the application which necessitates load capability and compliance interaction. Inspired by the musculocutaneous system, we combine both smart and compliant materials to construct an SRM, as shown in Figure 2A, right, featuring the shape memory alloy (SMA) to mimic muscle and silicon substrate to emulate the properties of the skin. Different from traditional

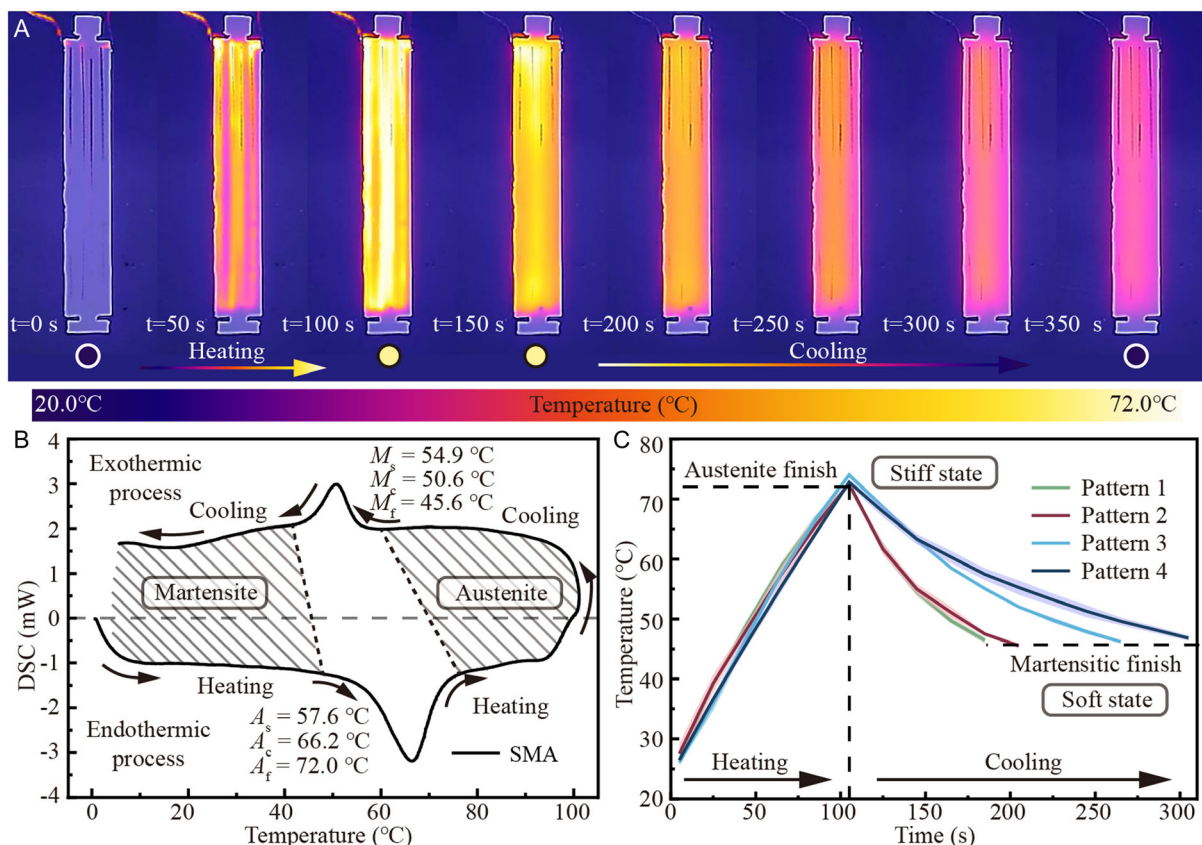


Figure 3. Thermomechanical properties of SRMs. A) SRM surface temperature timing sequence during heating and cooling. B) DSC results of SMA. C) Phase transformation processes of four patterns of SRMs.

SMA-driven soft robots, our SRM exhibits musculocutaneous-like stiffness-raising capabilities under the influence of Joule heating stimuli, thereby achieving stiffness regulation of soft machines.^[57,58] Concurrently, the silicon substrate maintains minimal contact stiffness, preserving its capability for compliant interaction. Since SMA is the primary factor in regulating structural stiffness,^[59] we arranged the SMA wires in configurations varying from 1 to 4 times, designed to achieve a proportional increase in structural stiffness. Here, according to the quantity of SMA, the SRMs exhibit four diverse arrangements, namely patterns 1–4. (The specific dimensions are shown in Figure S1, Supporting Information.)

3.2. Deformation Performance of SRMs

To evaluate the stiffness regulation performance of SRMs, we constructed a typical scenario, in which the SRMs act as a cantilever beam and are horizontally fixed by a clamp on one side. Here, we selected SRM with Pattern 4 as an example to quantify its stiffness regulation capability. When the weights ranging from 5 to 200 g are applied to our SRMs, we recorded the entire process of this experiment via a digital camera (FDR AX60, Sony, Japan) and then measured the longitudinal displacement y of the tip with the image software (ImageJ, National Institutes of Health, USA). We characterized the unstimulated state by Joule heat as a soft state, and the state induced by Joule heat, existing in the austenitic phase, as a stiff state. After affixing a 200 g weight, the cantilever beam, in its soft state, succumbs and assumes a nearly vertical posture, whereas it maintains functionality in the stiff state. Through the comparative analysis of

longitudinal displacements corresponding to identical weights, it is conspicuously observable that the apex displacement of the stiff state is diminished. In this test, the most significant effect is Pattern 4, which has markedly diminished displacement in the stiff state in contrast to the soft state (85.26 vs. 120.23 mm) (Figure 2D). Additionally, the exact terminal longitudinal displacements of the four patterns are enumerated in Table S1, Supporting Information. The results elucidate that the SRM manifests heightened bending stiffness and load-bearing capacity in the stiff state compared to the soft state; furthermore, the incorporation of additional SMAs within the soft plate amplifies the bending stiffness of our SRM.

3.3. Tunable Stiffness of the SRM

Upon the embedded SMA exceeding its intrinsic transformation temperature, our SRM undergoes a modifiable stiffening shift. Here, this temperature can be defined as the temperature at which it changes from martensite to austenite. This reversible modification can be instigated by the phase transition from austenite to martensite, reverting the material to its original state when the temperature descends below the transformation threshold. To elucidate the thermomechanical properties, infrared thermographic imaging (K20, HIKVISION, China) is utilized to record the temperature changes resulting from the application of 5.0 A current (with a voltage of around 1.5 V) to the SRMs, as depicted in Figure 3A (Video S1, Supporting Information). Upon stimulation with 5.0 A current, the SMA experiences an increase in temperature; however, it remains within the designated service temperature parameters of the silicon substrate, which span

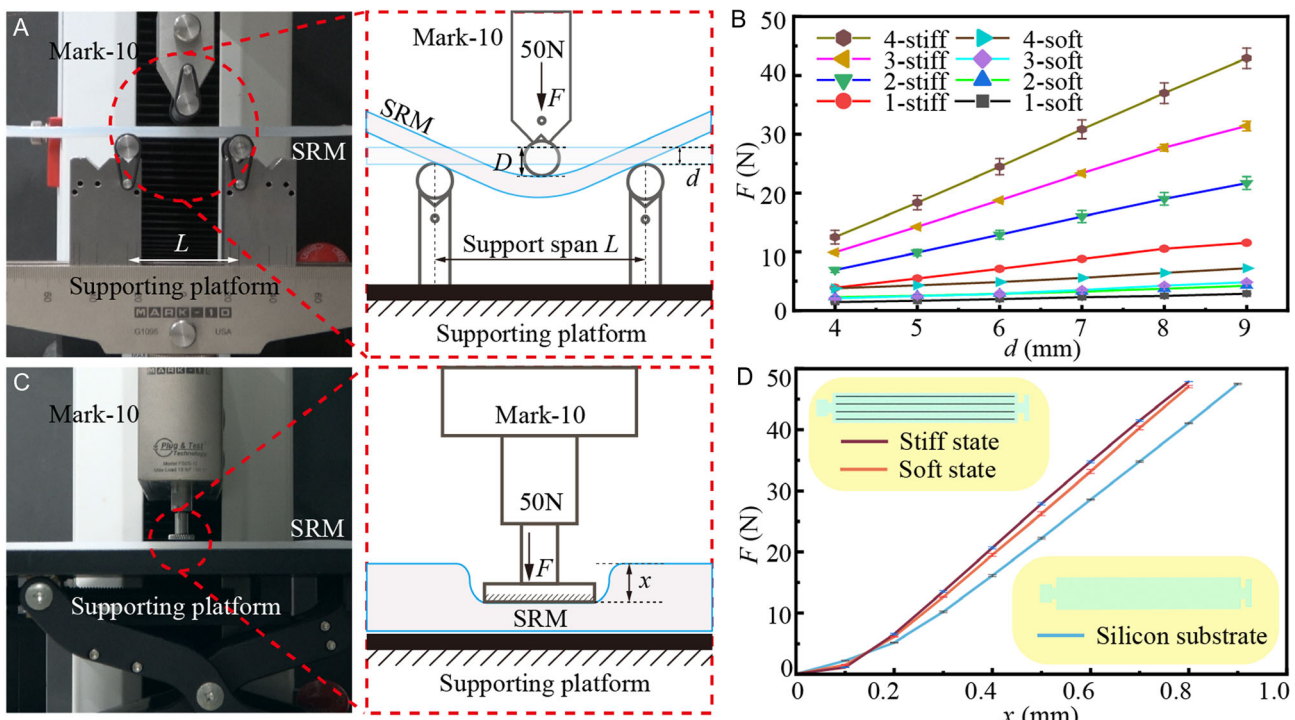


Figure 4. Three-point bending and compression tests of SRM. A) Experimental setup of the three-point bending test. B) The linear region of the force–displacement trajectory. C) Experimental setup and D) the corresponding results of the compression test.

from -53 to $+232$ $^{\circ}\text{C}$. Then, to elucidate the phase transition mechanisms of our SRM under stimulation, DSC experiments are performed on the SMA samples, and the experimental results are demonstrated in Figure 3B. The data represent the phase transition temperatures of the SMA, which corresponds to the phase transition thresholds of our materials. Specifically, the austenite starts (A_s) at 57.6 $^{\circ}\text{C}$ and finishes (A_f) at 72.0 $^{\circ}\text{C}$ during Joule heat stimulation. In the cooling phase, we discover that the transformation of the martensite starts at 54.9 $^{\circ}\text{C}$ (M_s) and finishes at 45.6 $^{\circ}\text{C}$ (M_f).

Consequently, we segment the entire thermodynamic behavior of SRMs into two stages, respectively, namely, the stimulation stage and the heat exchange stage. During the stimulation phase, the application of 5.0 A current to the SMA induces Joule heating, which serves as the stimulation mechanism, elevating the material's temperature from room temperature (25 $^{\circ}\text{C}$) to A_f . Upon converting Joule heat into phase transition potential energy, the state of our materials switches into austenite from martensite. In Figure 3C, despite the four configurations exhibiting distinct resistance values, their corresponding voltages similarly manifest a multiplicative correlation due to the multiplicative relationship with the quantity of SMA filaments. Consequently, each configuration can undergo a phase transition within 105 s. Regardless of its initial state, once subjected to the

specified current stimulation for 105 s, our SRM will transition to the rigid state. This characteristic ensures that we can determine its properties without the addition of inspection devices when it works in any complex conditions. Furthermore, we define the cooling stage as a process after reaching the stiff state, in which the stimulation is removed and the SRM is allowed to show heat exchange until ambient conditions. Here, we discover that an increase in the number of wires within the SRM directly correlates with an extended duration of stiff state. For instance, pattern 4 sustains the stiff state for 200 s at this juncture, approximately doubling the duration observed in pattern 1. This difference is primarily attributed to the increased thermal mass, which results from a multiplicative number of SMAs. After ensuring the temperature and conversion characteristics of the SRMs' phase transition, it is necessary to evaluate both structural stiffness regulation and compliant interaction abilities.

To investigate the regulation capability in bending stiffness subsequent to Joule thermal stimulation, we execute a three-point bending examination on the SRM, as shown in Figure 4A (Video S2, Supporting Information). The materials of each configuration are pressed by 10 mm, and the corresponding force–displacement trajectory is measured, as shown in Figure 4B. We opt for the quantification of the statistical stiffness within the moderately stable linear segment (displacement

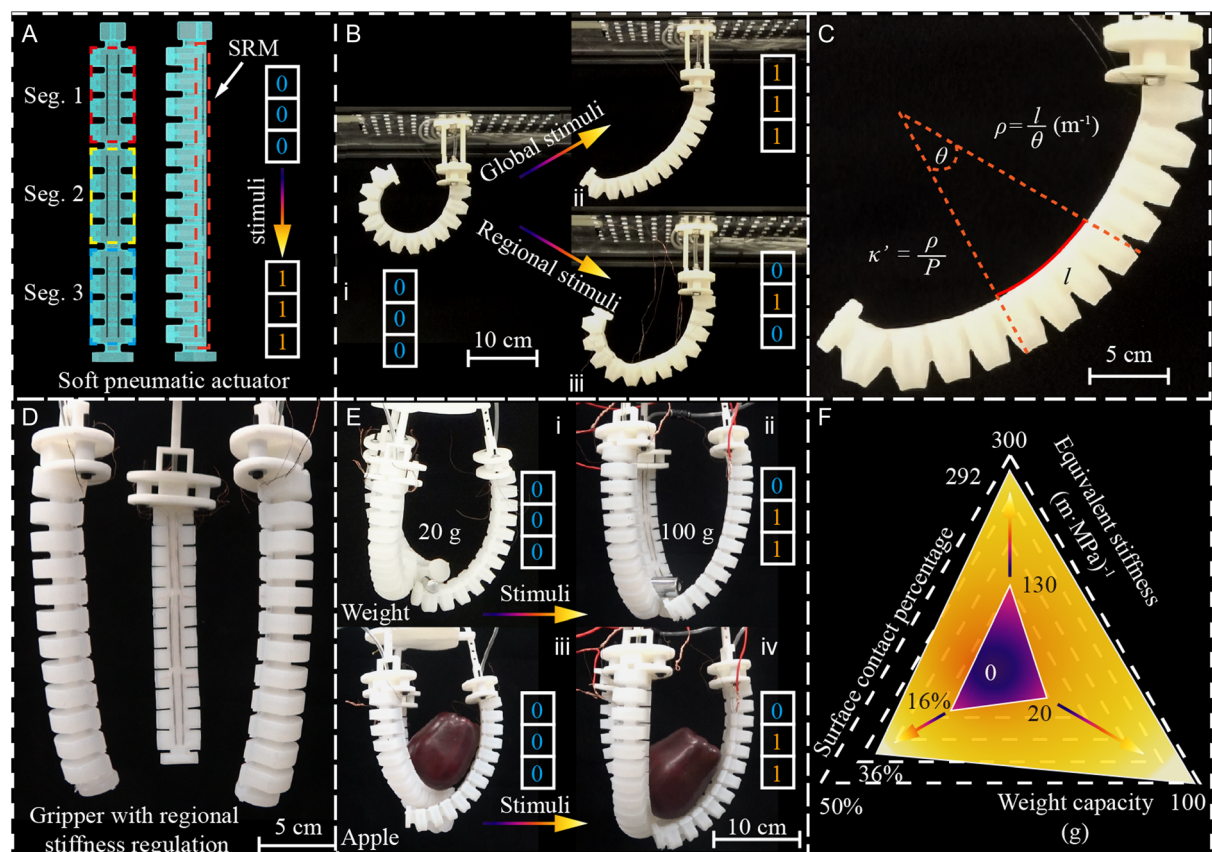


Figure 5. Soft gripper-integrated SRM for achieving regional stiffness regulation. A) SPA embedded with SRM. The soft and rigid stiffness can be denoted as 0 and 1, respectively. B) Configuration changes of SPA by applying two stimuli strategies. C) Definition of curvature radius and equivalent stiffness. D) Configuration of soft gripper. E) Maximum load and surface contact percentage of soft gripper pre- and poststimulation. F) Properties' quantification of gripper pre- and poststimulation.

interval of 4–9 mm) to be performed via numerical fitting. The corresponding flexural rigidities are shown in Table S2, Supporting Information. In this linear regime, the apex of displacement at 9 mm exhibits a substantial increase in maximal load endurance, escalating from 2.8 to 43 N, an amplification factor of ≈ 15 . This load endurance is consistent with an escalation in flexural modulus, which rises from 6.6 to 142.4 MPa, reflecting a multiplication of ≈ 21.5 times. These mechanical properties align precisely with the requirements ranges of soft robotics, rendering SRM a viable contender for structural stiffness modulation within the domain of soft machines.

We further showcase the application for gentle manipulation by quantifying the deformation of our materials in both stiff and soft states (Figure 4C, Video S3, Supporting Information). We gauge the contact stiffness of Pattern 4 with maximal stiffness (stiff state), and minimal stiffness (soft state), then compare them against a pure silicone substrate devoid of SMAs. According to the fitted curves displayed in Figure 4D, the

findings disclose the Young's modulus of around 2.20 MPa, virtually in parity with the 1.95 Young's modulus of the silicon substrate. For example, after compressing pattern 4 to a displacement of 0.8 mm, the contact force in the stiff state is 47.89 N, which is only 0.8 N more than the soft state (47.09 N). These results demonstrate the SRM's proficiency in regulating structural stiffness while preserving environmental compliance and interaction capabilities.

3.4. Application Demonstration

To illustrate the functionality of the SRM more comprehensively in soft machine applications, we first fabricate soft pneumatic actuators (SPAs) integrating the above material as a constraining layer, by which the structural stiffness can be programmed. As shown in Figure 5A, to modulate regional stiffness, we divide the SRM into three segments (i.e., Pattern 2) extending from the

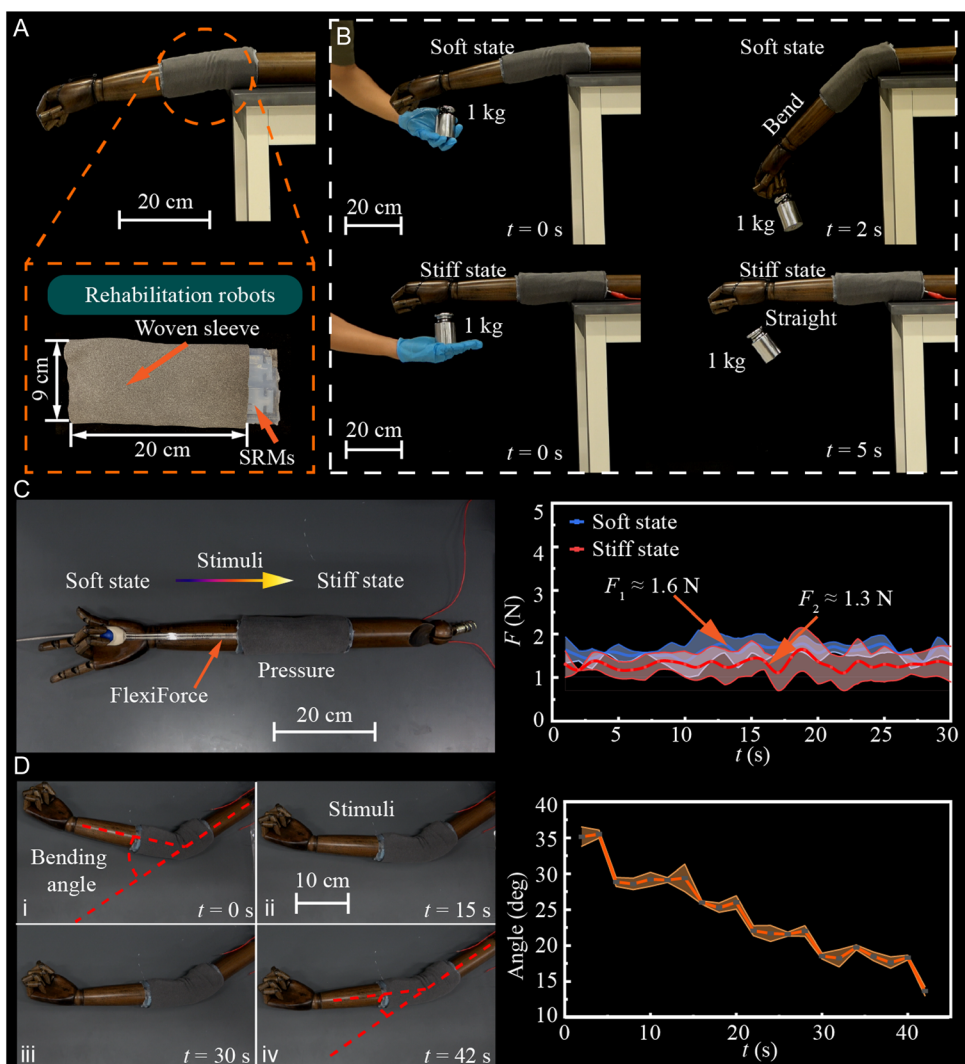


Figure 6. SRM-based wearable device. A) Experimental setup is composed of a prosthesis limb and a wearable device. B) Bending performance of the wearable device. i–iv) Loading evaluation for both soft and stiff states. C) Contact force comparison between soft and stiff states. D) Demonstration of the actuation performance of the wearable device.

base to the end, named Seg. 1–3. As depicted in Figure 5B, we administer two distinct types of stimulation: global and regional, respectively, to activate the SRM, thereby inducing it transition to a rigid state. Here, acknowledging the binary nature of the structural stiffness status for each segment, we can characterize a segment capable of transitioning between a soft state (designated as 0) and a rigid state (designated as 1). Such a result reveals that when the segments are stimulated, the corresponding bending deformation will be constrained, thereby diminishing the local curvature. To further quantify the capability of structural stiffness regulation, we define the bending curvature $\rho = l/\theta$ and equivalent structural stiffness of the SPA, which can be calculated according to $\kappa' = \rho/P$, as shown in Figure 5C. We discover that the equivalent structural stiffness relative to its initial soft state exhibited an augmentation of nearly 2.2 times upon stimulation of the limiting layer. Then, we arrange three SPAs in parallel to construct a soft robotic gripper, as shown in Figure 5D. We quantify the load-bearing and conformal interaction capabilities of the robotic gripper to evaluate the grasping performance of the gripper (Video S4, Supporting Information). When the current is applied to the soft gripper, the local stiffness of the soft gripper exhibits the equivalent stiffness of 292 (m MPa)^{-1} , which is 2.2 times that in the soft state. The increased structural stiffness enables the robotic gripper to resist stronger disturbances and achieve robust structural shape retention, by which its load-bearing capability can be improved. For example, the maximum capacity goes up to 100 g, which is about 5 times that of the soft state. Moreover, using stiffness regulation

strategies, our robotic gripper can grasp items conformally due to the enhanced regional structural stiffness, thus achieving a higher contact percentage. This percentage, which we define as the proportion of the gripper's contact profile to the items' profile, increases from 16.0% to 36.0%.

In the second application, we utilized our SRM to develop an assistance device for patient rehabilitation. In terms of medical machines and wearable devices, most efforts are focused on power, actuation, and control, while neglecting the compliance of the device's interaction with tissues.^[60,61] These devices, composed of hard materials, cannot interact with humans compliantly, which may result in poor treatment or even secondary injury.^[62] Here, we create a wearable device by integrating SRMs with a heat-insulating woven sleeve, as demonstrated in Figure 6A. This proposed concept allows for a light and thin paradigm, extending on the surface that can easily wrap a limb. To showcase the immobilization and protective features for injured limbs, we create a specific scenario where the prosthetic limb is arranged horizontally on the table to securely hold a 1 kg weight (Figure 6B). In the soft state, the wearable device does not restrict the normal movement of the limbs, and the limbs bend immediately after grabbing the weight. When stimulated, the wearable device switches to the stiff state, and no bending occurs after grabbing the weight, thus effectively fixing the patient's limbs (Video S5, Supporting Information). To illustrate the compliance properties of this device, we apply a pressure sensor (FlexiForce, Tekscan, Inc, USA) to measure the contact force between the wearable device and the prosthesis before and after

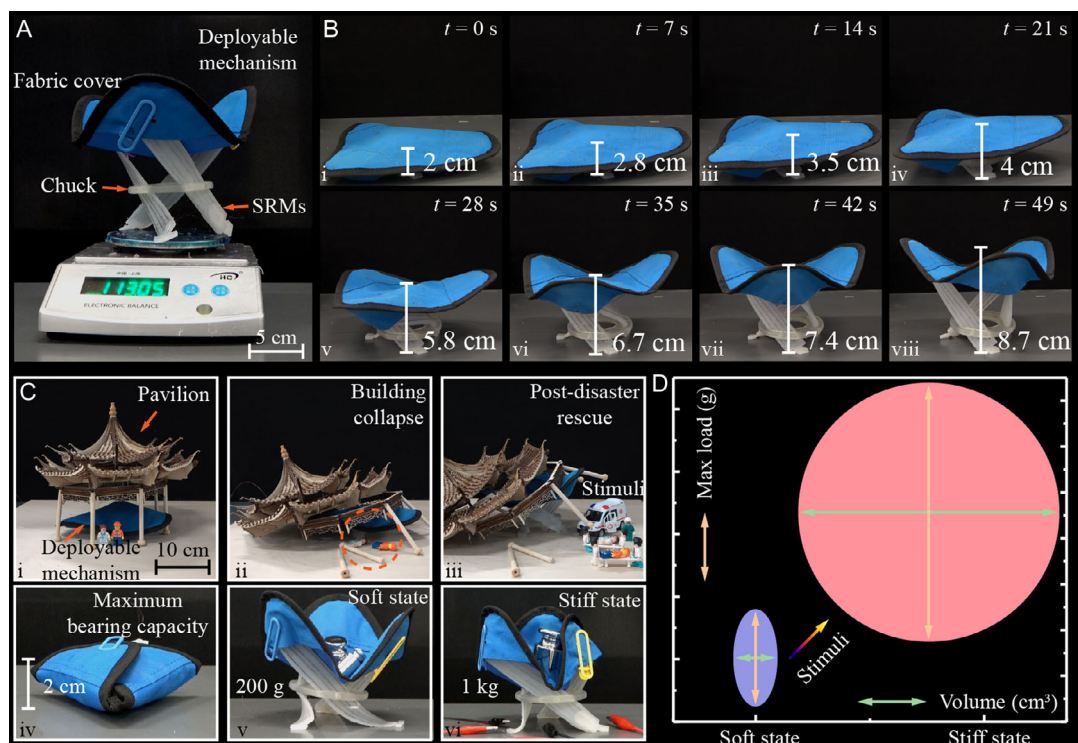


Figure 7. Application of SRMs in a deployable mechanism for postdisaster rescue. A) Configuration of the deployable mechanism. B) Snapshots of the unfolding process of the deployable mechanism under stimulation. C) Deployable mechanism for postdisaster rescue. i–iii) Rescue procedure after building collapse. iv–vi) Folding and loading evaluation for the mechanism. D) Volume and maximum load of the deployable mechanism.

stimulation (Figure 6C). We discover that the force of this stimulated device on the human body is only around 1.3 N, and the corresponding pressure is only 72 Pa, which is consistent with the soft state. Therefore, we consider that our device not only immobilization and is protective for injured limbs, but provides a compliant and comfortable choice. In addition, we also discover that our wearable device has a tendency to change from bent to straight after stimulation, which can also be applied as an actuator to perform rehabilitation exercises for patients (Figure 6D).

We also implement a deployable mechanism utilizing three SRMs, a 3D-printed component, and a fabric cover, as illustrated in Figure 7A. Subsequently, Figure 7B elucidates the unfolding process of the mechanism when subjected to a stimulus. Notably, this mechanism converts into a supporting platform within 50 s. We quantify the height achieved during the unfolding sequence and determine the spatial occupancy of the deployable mechanism. The deployable mechanism initially encompasses a volume of 239.0 cm^3 , which expanded to 3444.7 cm^3 poststimulation. Here, the SRMs endow the mechanism with deployable characteristics and tunable carrying capacity (Video S6, Supporting Information). To demonstrate the improvement in volume and load-bearing capacity after stimulation, we constructed an unstructured environment typified by a building collapse that impedes rescue operations. After applying stimulation, the deployable mechanism lifts the broken debris, allowing the injured patient to be rescued. Additionally, its load-bearing capacity significantly increases to 1 kg, a notable enhancement to 8.8 times its own weight (113.1 g). This deployable mechanism, distinguished by its foldable nature and load-bearing qualities, may provide an effective route for equipment maintenance or structural support, such as post-disaster rescue.

4. Conclusion

In this study, inspired by the musculocutaneous system, we introduce a stimuli-responsive plate for effectively regulating the structural stiffness of soft machines. This innovation ensures that these machines consistently maintain contact stiffness, facilitating compliant interactions. Upon characterizing the mechanical performance, the flexural modulus experiences a significant elevation from 6.6 to 142.4 MPa with Joule heat stimulation, spanning two orders of magnitude. Concurrently, Young's modulus remains constant at 2.2 MPa during the programming of structural stiffness. The results reveal that, even when structural stiffness rises, our SRMs are capable of sustaining a lower contact stiffness for compliant interactions. Then, we construct three application scenarios integrated with SRMs, which are soft grippers, wearable devices, and deployable mechanisms, respectively. Experiment results demonstrate that by combining the SRM, these soft machines reach a higher structural stiffness without sacrificing the contact stiffness, thereby enabling higher load capabilities. In future work, we would like to integrate additional advanced materials to further reduce both the temperature and the duration of the phase transition. Moreover, by incorporating temperature-responsive, tactile, and strain-sensing hydrogels, we aim to achieve self-sensing capabilities in SRMs.

Supporting Information

Supporting Information is available from the Wiley Online Library or from the author.

Acknowledgements

K.M. and J.Z. contributed equally to this work. This work was supported by the Shenzhen Science and Technology Program (grant nos. GXWD20201231165807008 and 20200830220051001) and the National Natural Science Foundation of China (no. 52275298).

Conflict of Interest

The authors declare no conflict of interest.

Data Availability Statement

The data that support the findings of this study are available from the corresponding author upon reasonable request.

Keywords

consistent contact stiffness, soft machines, stimuli-responsive material, structural stiffness regulation

Received: February 23, 2024

Revised: April 9, 2024

Published online:

- [1] S. Li, H. Bai, R. F. Shepherd, H. Zhao, *Angew. Chem. Int. Ed.* **2019**, *58*, 11182.
- [2] R. V. Martinez, J. L. Branch, C. R. Fish, L. Jin, R. F. Shepherd, R. M. D. Nunes, Z. Suo, G. M. Whitesides, *Adv. Mater.* **2013**, *25*, 205.
- [3] R. Deimel, O. Brock, *Int. J. Rob. Res.* **2016**, *35*, 161.
- [4] M. Wehner, M. T. Tolley, Y. Mengüç, Y.-L. Park, A. Mozeika, Y. Ding, C. Onal, R. F. Shepherd, G. M. Whitesides, R. J. Wood, *Soft Rob.* **2014**, *1*, 263.
- [5] P. Polygerinos, Z. Wang, K. C. Galloway, R. J. Wood, C. J. Walsh, *Rob. Auton. Syst.* **2015**, *73*, 135.
- [6] M. Cianchetti, T. Ranzani, G. Gerboni, T. Nanayakkara, K. Althoefer, P. Dasgupta, A. Menciassi, *Soft Rob.* **2014**, *1*, 122.
- [7] D. Rus, M. T. Tolley, *Nature* **2015**, *521*, 467.
- [8] J. Zhu, L. Lyu, Y. Xu, H. Liang, X. Zhang, H. Ding, Z. Wu, *Adv. Intell. Syst.* **2021**, *3*, 2100011.
- [9] J. Li, J. Cao, B. Lu, G. Gu, *Nat. Rev. Mater.* **2023**, *8*, 604.
- [10] W. Gao, J. Kang, G. Wang, H. Ma, X. Chen, M. Kadic, V. Laude, H. Tan, Y. Wang, *Adv. Intell. Syst.* **2023**, *5*, 2300285.
- [11] C. Majidi, *Adv. Mater. Technol.* **2019**, *4*, 1800477.
- [12] R. Pfeifer, M. Lungarella, F. Iida, *Commun. ACM* **2012**, *55*, 76.
- [13] X. Ke, J. Jang, Z. Chai, H. Yong, J. Zhu, H. Chen, C. F. Guo, H. Ding, Z. Wu, *Soft Rob.* **2022**, *9*, 613.
- [14] Y. Wang, J. Xiao, *Soft Matter* **2017**, *13*, 5317.
- [15] T. Mukhopadhyay, J. Ma, H. Feng, D. Hou, J. M. Gattas, Y. Chen, Z. You, *Appl. Mater. Today* **2020**, *19*, 100537.
- [16] K. Ma, X. Chen, J. Zhang, Z. Xie, J. Wu, J. Zhang, *IEEE Rob. Automation Lett.* **2023**, *8*, 2898.
- [17] J. Bernat, P. Gajewski, J. Kołota, A. Marcinkowska, *Appl. Sci.* **2023**, *13*, 1651.

- [18] G. Carreras, A. Isalgue, V. Torra, F. Lovey, H. Soul, *J. Therm. Anal. Calorim.* **2007**, 91, 575.
- [19] C. Auguet, A. Isalgue, V. Torra, F. C. Lovey, J. L. Pelegrina, *J. Therm. Anal. Calorim.* **2008**, 92, 63.
- [20] B. He, X. Dong, R. Nie, Y. Wang, S. Ao, G. Wang, *Mater. Des.* **2023**, 225, 111563.
- [21] K. Hou, J. Wu, X. Li, X. Zhang, Y. Sun, Y. Long, K. Song, *Adv. Mater. Technol.* **2023**, 8, 2201083.
- [22] J. Zhang, Y. Guo, W. Hu, R. H. Soon, Z. S. Davidson, M. Sitti, *Adv. Mater.* **2021**, 33, 2006191.
- [23] Y. Dong, L. Wang, N. Xia, Z. Yang, C. Zhang, C. Pan, D. Jin, J. Zhang, C. Majidi, L. Zhang, *Sci. Adv.* **2022**, 8, eabn8932.
- [24] J. Shintake, B. Schubert, S. Rosset, H. Shea, D. Floreano, in 2015 IEEE/RSJ Inter. Conf. on Intelligent Robots and Systems (IROS), Hamburg, Germany **2015**, pp. 1097–1102.
- [25] Y. Sheima, J. von Szczepanski, P. M. Danner, T. Künniger, A. Remhof, H. Frauenrath, D. M. Opris, *ACS Appl. Mater. Interfaces* **2022**, 14, 40257.
- [26] L. Ciarella, A. Richter, E.-F. Markus Henke, *Adv. Mater. Technol.* **2023**, 8, 2202000.
- [27] Z. Kang, L. Yu, Y. Nie, A. L. Skov, *ACS Appl. Mater. Interfaces* **2022**, 14, 51384.
- [28] C. Xiang, W. Li, Y. Guan, *Polymers* **2022**, 14, 4469.
- [29] Z. Noohi, S. Nosouhian, B. Niroumand, G. Timelli, *Metals* **2022**, 12, 945.
- [30] Y. Hao, J. Gao, Y. Lv, J. Liu, *Adv. Funct. Mater.* **2022**, 32, 2201942.
- [31] M. Behl, A. Lendlein, *Mater. Today* **2007**, 10, 20.
- [32] E. Hornbogen, *Adv. Eng. Mater.* **2006**, 8, 101.
- [33] A. Lendlein, S. Kelch, *Angew. Chem. Int. Ed.* **2002**, 41, 2034.
- [34] C. Liu, H. Qin, P. T. Mather, *J. Mater. Chem.* **2007**, 17, 1543.
- [35] Y.-F. Zhang, N. Zhang, H. Hingorani, N. Ding, D. Wang, C. Yuan, B. Zhang, G. Gu, Q. Ge, *Adv. Funct. Mater.* **2019**, 29, 1806698.
- [36] B. Aksoy, H. Shea, *Adv. Funct. Mater.* **2020**, 30, 2001597.
- [37] N. El-Atab, R. B. Mishra, F. Al-Modaf, L. Joharji, A. A. Alsharif, H. Alamoudi, M. Diaz, N. Qaiser, M. M. Hussain, *Adv. Intell. Syst.* **2020**, 2, 2000128.
- [38] J. Zhang, B. Wang, H. Chen, J. Bai, Z. Wu, J. Liu, H. Peng, J. Wu, *Adv. Mater. Technol.* **2023**, 8, 2201616.
- [39] Y. Zhao, Z. Zhang, Z. Ling, X. Gao, X. Fang, *Appl. Therm. Eng.* **2022**, 217, 119202.
- [40] Y. Yang, Y. Chen, Y. Li, M. Z. Q. Chen, Y. Wei, *Soft Rob.* **2017**, 4, 147.
- [41] S. Namathoti, R. K. V.M., R. S. P.S., *Mater. Today: Proc.* **2022**, 56, 1182.
- [42] A. A. Ameen, A. M. Takhakh, A. Abdal-hay, *Eur. Polym. J.* **2023**, 194, 112145.
- [43] D. Shen, Q. Zhang, Y. Han, C. Tu, X. Wang, *Soft Robotics* **2023**, 10, 1015.
- [44] Y. S. Narang, J. J. Vlassak, R. D. Howe, *Adv. Funct. Mater.* **2018**, 28, 1707136.
- [45] Y. Wei, Y. Chen, Y. Yang, Y. Li, *Mechatronics* **2016**, 33, 84.
- [46] Y. Jiang, D. Chen, C. Liu, J. Li, *Soft Rob.* **2019**, 6, 118.
- [47] D. S. Shah, E. J. Yang, M. C. Yuen, E. C. Huang, R. Kramer-Bottiglio, *Adv. Funct. Mater.* **2021**, 31, 2006915.
- [48] Y. Li, Y. Chen, Y. Yang, Y. Wei, *IEEE Trans. Rob.* **2017**, 33, 446.
- [49] Y. Wei, Y. Chen, T. Ren, Q. Chen, C. Yan, Y. Yang, Y. Li, *Soft Rob.* **2016**, 3, 134.
- [50] J. Zhu, H. Chen, Z. Chai, H. Ding, Z. Wu, *Soft Rob.* **2023**.
- [51] J. S. Mohammed, W. L. Murphy, *Adv. Mater.* **2009**, 21, 2361.
- [52] Y. Yang, Y. Li, Y. Chen, *Bio-des. Manuf.* **2018**, 1, 14.
- [53] D. R. Higuera-Ruiz, K. Nishikawa, H. Feigenbaum, M. Shafer, *Bioinspiration Biomimetics* **2021**, 17, 011001.
- [54] S. Wei, T. K. Ghosh, *Adv. Mater. Technol.* **2022**, 7, 2101521.
- [55] P. Egan, R. Sinko, P. R. LeDuc, S. Keten, *Nat. Commun.* **2015**, 6, 7418.
- [56] J. Xue, Y. Zou, Y. Deng, Z. Li, *EcoMat* **2022**, 4, e12209.
- [57] J. Hwang, W. D. Wang, *Adv. Mater. Technol.* **2022**, 7, 2101153.
- [58] J.-H. Lee, Y. S. Chung, H. Rodrigue, *Sci. Rep.* **2019**, 9, 11251.
- [59] P. S. Lobo, J. Almeida, L. Guerreiro, *Proc. Eng.* **2015**, 114, 776.
- [60] A. M. Dollar, H. Herr, *IEEE Trans. Rob.* **2008**, 24, 144.
- [61] W. Huo, S. Mohammed, J. C. Moreno, Y. Amirat, *IEEE Syst. J.* **2016**, 10, 1068.
- [62] R. K. Chen, Y. Jin, J. Wensman, A. Shih, *Addit. Manuf.* **2016**, 12, 77.